

Tuning Neuronal Circuit Formation in 3D Polymeric Scaffolds by Introducing Graphene at the Bio/Material Interface

Rossana Rauti, Nicola Secomandi, Cristina Martín, Susanna Bosi, Francesco P. U. Severino, Denis Scaini, Maurizio Prato,* Ester Vázquez,* and Laura Ballerini*


2D cultures are useful platforms allowing studies of the fundamental mechanisms governing neuron and synapse functions. Yet, such models are limited when exploring changes in network dynamics due to 3D-space topologies. 3D platforms fill this gap and favor investigating topologies closer to the real brain organization. Graphene, an atom-thick layer of carbon, possesses remarkable properties and since its discovery is considered a highly promising material in neuroscience developments. Here, elastomeric 3D platforms endowed with graphene cues are exploited to modulate neuronal circuits when interfaced to graphene in 3D topology. Ex vivo neuronal networks are successfully reconstructed within 3D scaffolds, with and without graphene, characterized by comparable size and morphology. By confocal microscopy and live imaging, the 3D architecture of synaptic networks is documented to sustain a high rate of bursting in 3D scaffolds, an activity further increased by graphene interfacing. Changes are reported in the excitation/inhibition ratio, potentially following 3D-graphene interfacing. A hypothesis is thus proposed, where the combination of synapse formation under 3D architecture and graphene interfaces affects the maturation of GABAergic inhibition. This will tune the balance between hyperpolarizing and depolarizing responses, potentially contributing to network synchronization in the absence of changes in GABAergic phenotype expression.

1. Introduction

The brain's ability to elaborate and store information relies on neural circuit topology. That is the way neurons are synaptically connected in a given network. The architecture of neural connectivity, therefore, is one of the crucial mechanisms enabling the emergence of a particular function from specific brain circuitries.^[1] Investigating the interplay between morphology and function in brain networks is an important yet challenging task limited, for example, by the overwhelming complexity of the intact central nervous system (CNS). Recently, the development of biomimetic 3D scaffolds has allowed to culture neuronal and glial cells within an interconnected porous structure, promoting the development of more complex 3D organizations of neuronal synaptic networks than in traditional monolayer conditions.^[2,3] We recently developed a 3D versatile platform that

Dr. R. Rauti^[+], Dr. N. Secomandi, Dr. F. P. U. Severino^[++],
Dr. D. Scaini, Prof. L. Ballerini
International School for Advanced Studies (SISSA/ISAS)
Trieste 34136, Italy
E-mail: laura.ballerini@sissa.it

Dr. C. Martín, Prof. E. Vázquez
Instituto Regional de Investigación Científica Aplicada (IRICA)
Universidad de Castilla-La Mancha
Avda Camilo José Cela, 13071 Ciudad Real, Spain
E-mail: ester.vazquez@uclm.es

 The ORCID identification number(s) for the author(s) of this article can be found under <https://doi.org/10.1002/adbi.201900233>.

^[+]Present address: Department of Biomedical Engineering, Tel Aviv University, Tel Aviv 69978, Israel

^[++]Present address: Cell Biology Department, Duke University Medical Center, Durham, NC 27710, USA

© 2020 The Authors. Published by WILEY-VCH Verlag GmbH & Co. KGaA, Weinheim. This is an open access article under the terms of the Creative Commons Attribution-NonCommercial-NoDerivs License, which permits use and distribution in any medium, provided the original work is properly cited, the use is non-commercial and no modifications or adaptations are made.

Dr. C. Martín, Dr. S. Bosi, Prof. M. Prato
Department of Chemical and Pharmaceutical Sciences
Università degli Studi di Trieste
Via Licio Giorgieri 1, Trieste 34127, Italy
E-mail: prato@units.it

Prof. M. Prato
Carbon Bionanotechnology Group
CIC biomaGUNE
Paseo Miramón 182, San Sebastián 20014, Guipúzcoa, Spain

Prof. M. Prato
Basque Foundation for Science
Ikerbasque, Bilbao 48013, Spain

Prof. E. Vázquez
Faculty of Chemical Science and Technology
Universidad de Castilla-La Mancha
13071 Ciudad Real, Spain

DOI: 10.1002/adbi.201900233

provides a cell-compatible elastomeric scaffold to be engineered for tissue formation. We further nanostructured such material with nanotopographies using multiwalled carbon nanotubes (MWCNTs).^[2,4] Decorating the elastomeric structure with nanomaterials exploits the scaffold properties at the interface, for example, guiding growth and adhesion of axons to the device or implementing the 3D construct of active components, such as electrically conductive pathways.^[4] Also, apart MWCNTs,^[2,5–7] many other carbon-based nanomaterials as, for example, graphene,^[8] may be used. This will provide artificial biomimetic cues able to affect synapse formation or neuronal information processing through the physical interactions of the nanomaterial with the biological environment. Hybridizing 3D biomimetic scaffolds with nanomaterials demonstrated to improve their cytocompatibility,^[9] their stability in vivo,^[4] and provides efficient tools to modulate biological processes.^[4,8] Graphene, a single atomic plane material made of sp²-hybridized carbon atoms, is characterized by peculiar properties, including high electrical conductivity, stiffness, electron mobility, mechanical flexibility, and optical transparency.^[10–13] The recent exploiting of graphene as a component of neural interfaces relies on the combination in a single material of all these features.^[14]

In neuroscience, flat graphene substrates were shown to promote axon sprouting and outgrowth,^[15] to reduce tissue inflammatory responses^[16,17] and, surprisingly, to enhance electrical signaling,^[8,18] highlighting graphene's potential as a tool for engineering neuronal interfacing devices.^[14,17,19–22] The translation of graphene capability to perturb neuronal network activity from 2D to 3D represents the next step in the design of artificial platforms for tissue engineering. Only a few studies report how graphene-based 3D constructs, yet with diverse graphene derived materials (from graphene foams to graphene oxide scaffolds), interact with biological tissue/cells and how the interfaced neuronal network responds when exposed to graphene in 3D.^[3,13,23,24] However, a detailed characterization of neural circuit adaptation to a 3D graphene environment is currently missing. Here, we took advantage of self-standing elastomeric scaffolds, characterized by a microporosity able to shape a functional 3D neuronal network,^[2] to create a condition where neuronal cells could interact with single layer graphene in a genuine 3D environment. We studied intracellular calcium activity in neurons within 3D hippocampal cultures that differed only by their being interfaced to graphene or not, providing evidence that, despite the similar cellular composition and morphology of the resulting 3D neuronal networks, graphene has the ability to alter the synaptic inhibitory control of the emerging synaptic activity. Surprisingly this effect seems intrinsic of the 3D topology since in 2D it is not present.

2. Results

2.1. Fabrication and Characterization of 3D Scaffolds

We present here a microporous, self-standing elastomeric-scaffold whose facets are covered by graphene and able to sustain the development of a genuine 3D-network of cells from rat hippocampus. Control 3D scaffolds consisting of polydimethylsiloxane (PDMS) alone were fabricated following a pre-

viously described procedure.^[2,4] Briefly, the scaffold was made of PDMS with micrometric cavities generated by the dissolution of a sugar template after that all interstitial space was previously embedded by the elastomer and cured. To exploit the ability of graphene to impact a 3D neuronal circuit, we modified the pristine 3D PDMS scaffold fabrication procedure by mixing few-layer graphene flakes with the sugar. This produces an agglomerate with graphene flakes layered on all sugar grains' faces. After PDMS infiltration and curing, sugar dissolution leaves graphene flakes partially embedded, and consequently trapped, at the surface of the PDMS scaffold resulting in 3D PDMS-graphene (3D-PDMS-GR) samples. The starting graphene flakes were fully characterized by thermogravimetric analysis (TGA), Raman spectroscopy, and transmission electron microscopy (TEM) (Figure 1A–C). A low number of defects/functional groups characterize the graphene surface as pointed out by TGA analysis (Figure 1A) while Raman spectroscopy shows a ratio between the intensities of D and G bands (I_D/I_G) of 0.42 (Figure 1B). These two results indicate that the starting graphene material consists of about 4 layers of graphene flakes.^[25–27] TEM analysis, on the other hand, shows that the distribution of lateral dimensions of the flakes, based on a gaussian fit, is centered around 304 ± 124 nm (Figure 1C).

The presence of graphene flakes trapped within 3D PDMS-GR was assessed by Raman spectroscopy. An example of a typical Raman profile acquired within a pore of a 3D PDMS-GR scaffold is displayed in Figure 1D (average of 25 consecutive spectra) where graphene characteristic tangential (G, ≈ 1580 cm⁻¹), disordered (D, ≈ 1350 cm⁻¹), and second order (2D, ≈ 2700 cm⁻¹) peaks are clearly visible,^[28] together with two very intense bands around 3000 cm⁻¹ which correspond to the methyl symmetric and asymmetric stretching vibrations (\parallel and \perp , respectively) of the PDMS.^[29] In Figure 1E we show a 3D mapping of the G-band intensity within a parallelepiped extending from the surface of the scaffold to 10 μ m in depth by steps of 1 μ m. A total of 4290 spectra were represented in the 3D representation and a color code was chosen to represent G-band intensity (red for higher intensities). From this, we were able to chemically visualize graphene on PDMS scaffold facets, confirming the presence of a homogeneous distribution of graphene flakes trapped within the scaffold surface.

We aimed at a system developed to allow the growth (within a 3D environment) of a neuronal network directly interfaced with graphene and, at the same time, soft enough to resemble the compliance of neural tissues. Using a high-resolution compressive load-cell we measure, by uniaxial-load compression test (see the Experimental Section), an indicative E value of 59.10 kPa for the 3D PDMS scaffold and of 58.82 kPa for the 3D PDMS-GR one (Figure 1F). The two values, obtained calculating the initial linear slope of the corresponding stress–strain curve, are very similar, highlighting the absence of alterations in the bulk mechanical properties due to the superficial layering of graphene.

The electrical characterization (see the Experimental Section) of the graphene enriched PDMS scaffold was performed as a function of scaffold deformation squeezing the sample between two conductive, flat, electrodes (Figure 1G, left). Our analysis pointed out the necessity to induce at least a 20% deformation in the 3D PDMS-GR scaffold to start having a measurable value of resistivity (4.7 G Ω mm). Not surprisingly, resistivity

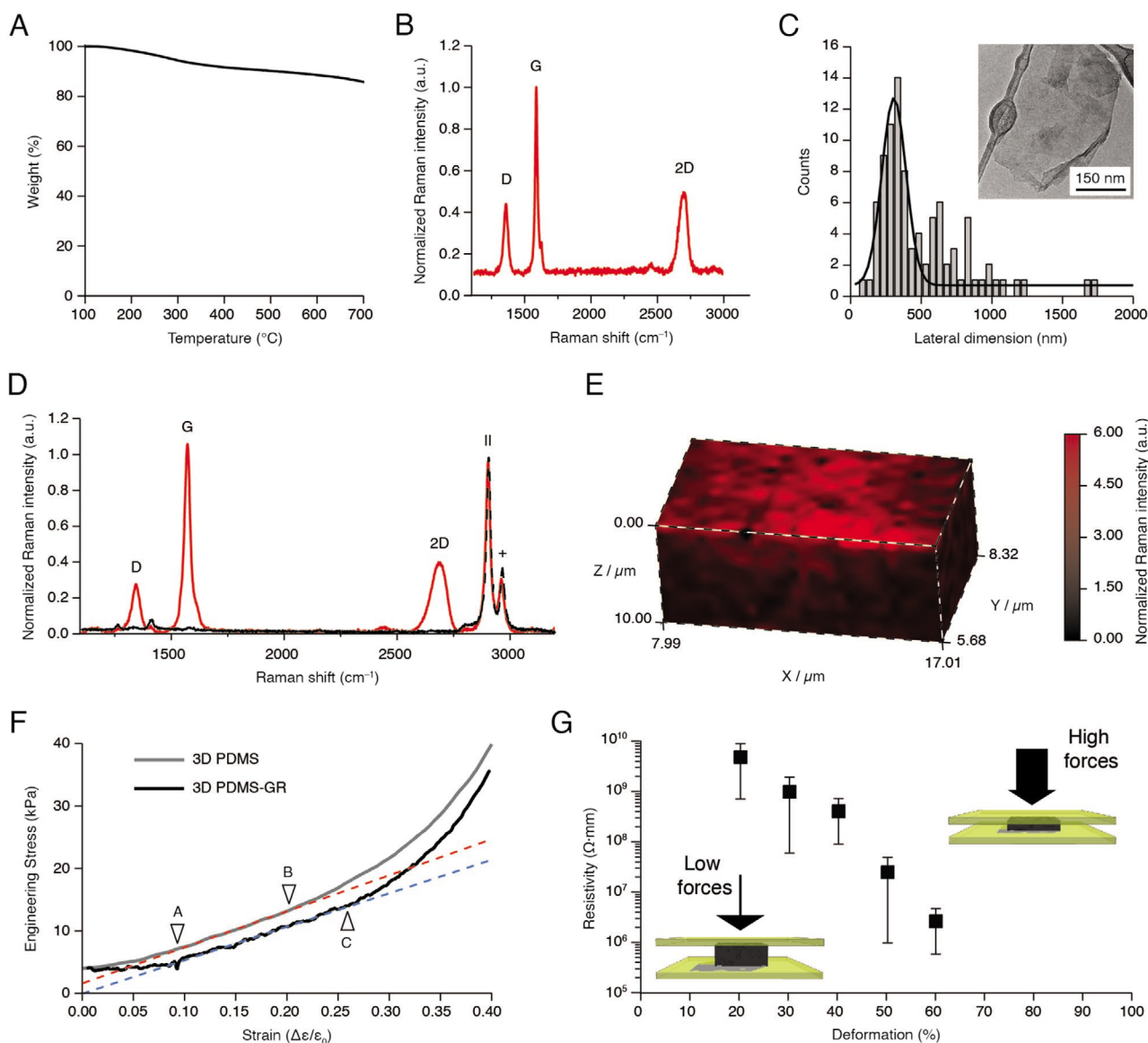


Figure 1. Physicochemical characterization of the few-layer graphene and the 3D PDMS-Gr scaffold used in this study. A) Thermogravimetric analysis (repeated twice) and B) Raman spectroscopy (average spectrum of at least 20 individual spectra) of the starting few-layer graphene flakes used. C) Lateral size distribution of graphene flakes determined from transmission electron microscopy (TEM) observations (in the inset a representative image is shown). D) Average Raman spectrum obtained from 25 different point measurements performed within a pore of a 3D PDMS-Gr scaffold (in red, solid), compared with a Raman spectrum acquired on a 3D PDMS scaffold (in black, dashed). Graphene characteristics tangential (G), disordered (D), and second order (2D) peaks were shown. PDMS has two strong peaks at 2905 and 2960 cm^{-1} corresponding to the symmetric (||) and antisymmetric (+) $-\text{CH}_3$ stretching vibrations. E) Perspective of a G-band intensity Raman 3D mapping of the interior of a 3D PDMS-Gr pore. The reddest regions evidence the higher presence of graphene. F) Stress–strain plots for a 3D PDMS scaffold (in gray) and for a 3D PDMS-Gr scaffold (in black). Elastic moduli (E) (about 60 kPa in Young’s modulus for both materials) were determined from the initial linear slope of the corresponding stress–strain curves (in red, from A to B strain values, for 3D PDMS; in blue, from A to C strain values for 3D PDMS-Gr). G) Deformation-dependent resistivity measurements of a 5 mm side size cube of 3D PDMS-Gr scaffold. The scaffold was compressed between two flat electrical contacts recording its resistivity under variable values of applied forces (initial F_0 was 50 mN and increased until a maximum 60% deformation was achieved, see the Experimental Section for details). The resistivity versus deformation plot shows a decrease in resistivity as the scaffold is compressed between the two flat contacts. Has to be noted that a minimum 20% deformation has to be reached before being able to measure a resistivity value.

value decreased monotonically as deformation was increased, reaching a final value of about 2.7 $\text{M}\Omega \text{ mm}$ at 60% deformation (Figure 1G, right plot).

The general morphologies of both 3D PDMS and 3D PDMS-Gr scaffolds were compared by scanning electron microscopy

(SEM) reconstructions (Figure 2A, left and right, respectively). SEM analysis revealed very similar morphologies for the two scaffolds and showed that sugar crystals dissolution generates faceted interconnected pores, which allow networks of channels within the PDMS matrix. The diameter of the pores within the

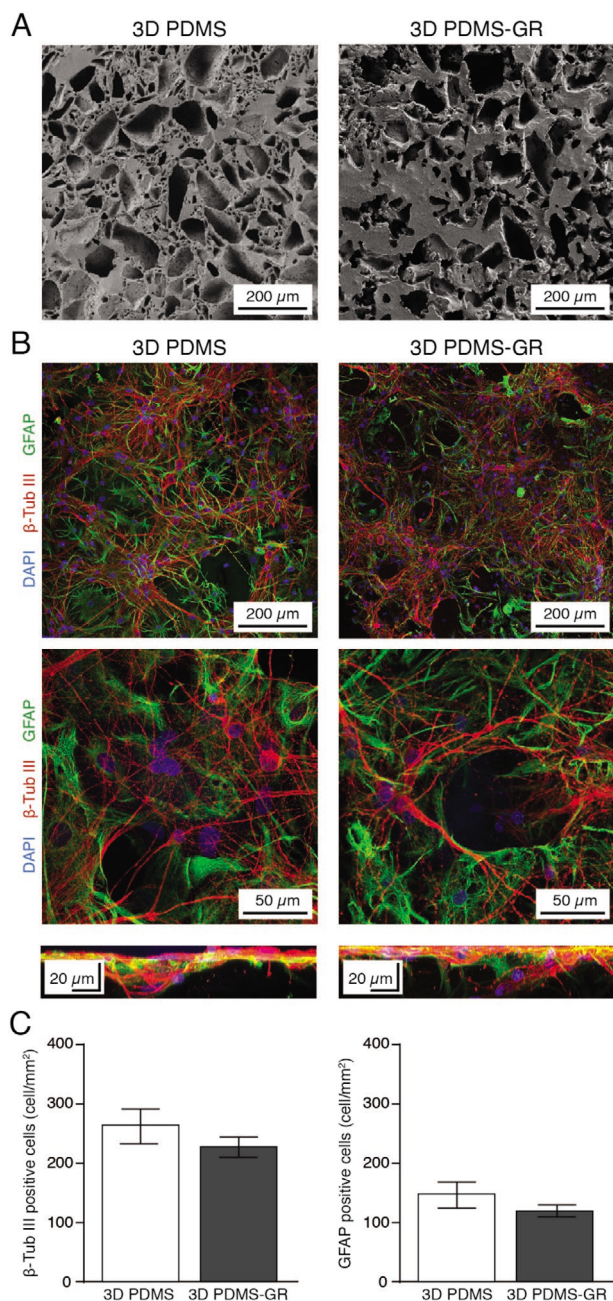


Figure 2. Development of primary neurons in 3D PDMS and 3D PDMS-GR scaffolds. A) Low magnification SEM images of 3D PDMS and 3D PDMS-GR scaffolds (left and right, respectively); note the similar morphology and cavity size distribution between the two materials. B) Confocal micrographs at low (first row) and high (second row) magnification showing hippocampal cultures grown (10 days) within a 3D PDMS scaffold (left) and a 3D PDMS-GR one (right). Cells were immune-stained for neurons (anti β -tubulin III, in red), glial cells (anti GFAP, in green), and nuclei (DAPI, in blue). Note the complex growth of neuronal and glial processes exposed to the third dimension. To highlight the genuine 3D cellular networks developed within the two porous scaffolds lateral z views from the 3D images were shown (third row). C) Bar plots summarizing the neuronal (left) and glial (right) cell densities in the two constructs.

two scaffolds was evaluated in the range of 100–200 μm in both conditions, although 3D PDMS-GR scaffolds' surfaces are covered by graphene flakes, as pointed out by Raman spectroscopy (Figure 1D,E).

2.2. Self-Standing PDMS Scaffolds Sustain Hippocampal Cells Growth in 3D: Functional Impact of Few-Layer Graphene

To investigate the development of neuronal networks when interfaced in the third dimension to graphene, we seeded rat dissociated hippocampal cells in the two elastomeric microporous scaffolds,^[2,30] named 3D PDMS and 3D PDMS-GR, whose structure and porosity are shown in the representative SEM images of Figure 2A. The cell composition and 3D organization of cultured hippocampal tissues within the two scaffolds were assessed after 9–11 days *in vitro* (DIV) by confocal microscopy of β -tubulin III and glial fibrillary acidic protein (GFAP) immunofluorescence labeling, to visualize cytoskeletal components selective for neurons and astrocytes, respectively (Figure 2B).^[31–34] In all cultures tested for confocal reconstruction ($n = 8$ for 3D PDMS and $n = 7$ for 3D PDMS-GR), prior to microscopy analysis, neuronal calcium activity was monitored (see below) and at the end of each recording session, the samples were fixed and processed for microscopy. Representative confocal micrographs at low (Figure 2B, first row) and high (Figure 2B, second row) magnifications highlight the formation of a genuine 3D configuration of neurons and glial cells when developed sustained by the 3D PDMS (left) and 3D PDMS-GR (right) scaffolds. To highlight the topology of the 3D networks into the two porous scaffolds, we extrapolated from the 3D confocal images obtained by zeta stacking, the zeta profile reconstructions (Figure 2B, bottom panels). In both conditions (3D PDMS and 3D PDMS-GR), an effective growth along the z-axis is depicted confirming that these scaffolds promote 3D cellular network formation, where neurons and glial cells are disposed on different levels, as also disclosed by cell nuclei distribution (in blue).^[2,30] We further quantified the hippocampal cell density which did not differ in the two conditions for both neurons (3D PDMS: 262.3 ± 29.2 β -tubulin positive cells mm^{-2} ; 3D PDMS-GR: 227.9 ± 16.4 β -tubulin positive cells mm^{-2}) and astrocytes (3D PDMS: 146.8 ± 18.6 GFAP positive cells mm^{-2} ; 3D PDMS-GR: 118.4 ± 9.2 GFAP positive cells mm^{-2} ; $n = 28$ visual fields in 3D PDMS and $n = 23$ visual fields in 3D PDMS-GR, four independent culture series; bar plots in Figure 2C). Cytocompatibility, together with the ability to instruct a 3D culture formation, were thus confirmed for the 3D PDMS platforms and our results suggest that decorating scaffold pores' surfaces by a thin film of few-layers graphene flakes did not alter the resulting cellular network in size and morphology.^[2]

Primary cultured neurons once reorganized *ex vivo* in 3D scaffolds are known to develop functional synaptic connections and circuits characterized by the spontaneous generation of temporally structured electrical activity.^[2] We explored the network dynamics in 3D PDMS and 3D PDMS-GR by calcium imaging with fluorescent indicators. This is a minimally

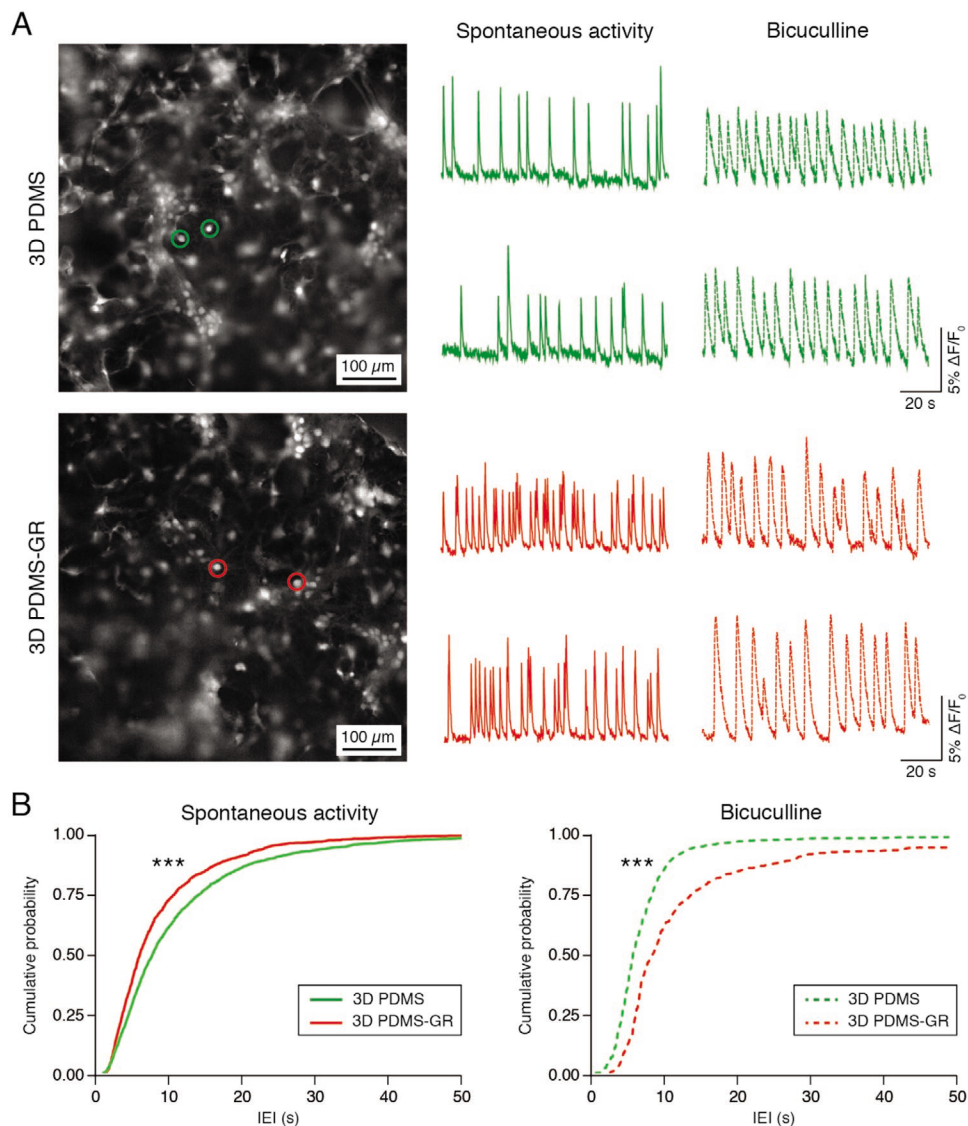


Figure 3. Live calcium imaging of network activity in 3D PDMS and 3D PDMS-GR. A) Snapshots of representative fields of neuronal cultures grown on 3D PDMS and 3D PDMS-GR stained with the Oregon Green 488-BAPTA-1 AM calcium indicator. Fluorescence tracings represent repetitive Ca^{2+} -events spontaneously (plain traces) or bicuculline induced (dotted traces) recorded in hippocampal cultures (two sample neurons were selected from the same field) in the two culturing conditions (3D PDMS, in green; 3D PDMS-GR, in red). B) Cumulative probability plots of the distribution of interevent interval (IEI) values within 3D PDMS and 3D PDMS-GR neuronal networks in saline solution (left) and upon removal of synaptic inhibition by bicuculline (right). (Kolmogorov–Smirnov test; 5 different series of cultures, $***p < 0.001$.)

invasive approach that allows monitoring calcium transients in neuronal populations at single-cell resolution.^[2,3,30,35] Neurons, stained with the membrane-permeable Ca^{2+} dye Oregon Green 488 BAPTA-1, were simultaneously visualized within the sampled area (visual field $680 \times 680 \mu\text{m}^2$; **Figure 3A**, left fields of view) and on average 30 ± 12 fluorescent cells were isolated and imaged in each visual field (see the Experimental Section). In these recordings, repetitive and spontaneous Ca^{2+} events were detected in 77% (555 out of 723 neurons, $n = 23$ visual fields, 3D PDMS) and, similarly, in 79% (705 out of 894 neurons, $n = 24$ visual fields; 3D PDMS-GR cultures) of visualized neurons. In **Figure 3A**, right, sample tracings of spontaneous fluorescent recordings from active cells are depicted for comparison between 3D PDMS (in green) and 3D PDMS-GR (in red)

cultures. Spontaneous and bicuculline ($10 \times 10^{-6} \text{ M}$; a competitive antagonist of GABA_A receptors) sustained activity of two representative cells were shown for each condition. Calcium events are usually due to spontaneous episodes of synaptic, action potential-dependent, bursts of activity, fully blocked by Tetrodotoxin (TTX, $1 \times 10^{-6} \text{ M}$; a blocker of fast voltage dependent Na^+ channels; see the Experimental Section) applications. We quantified the occurrence of spontaneous Ca^{2+} episodes in active cells by measuring the interevent interval (IEI), the time interval between the onset of a calcium burst and the beginning of the next one. IEI was significantly ($***p < 0.001$; Kolmogorov–Smirnov test) shorter in 3D PDMS-GR cultures ($9.8 \pm 0.18 \text{ s}$, $n = 175$ cells, from 5 different series of cultures) when compared to 3D PDMS ones ($12.7 \pm 0.23 \text{ s}$, $n = 208$ cells,

from 5 different series of cultures; see the IEI cumulative distribution in Figure 3B, left plot). We further quantified network synchronization by evaluating the mean cross correlation factor (CCF; see the Experimental Section) of spontaneous calcium episodes. 3D PDMS cultures displayed a CCF value of 0.48 ± 0.04 ($n = 14$ fields) significantly ($***p < 0.006$, Mann Whitney test) smaller than the value detected in 3D PDMS-GR (CCF 0.66 ± 0.04 ; $n = 13$ fields), indicative of a higher synchronization among active neurons when interfaced to graphene in the third dimension. All these results suggest increased neuronal excitability or diverse paths of neuronal interconnection, for example displaying a lower synaptic inhibition, when neurons are interfaced with graphene in 3D constructs.

In neuronal circuits, the ratio of excitatory and inhibitory inputs to a cell usually regulates the balance between excitation and inhibition. To gain insights into the GABAergic inhibitory control of the neural circuits developed in the two 3D scaffolds, we compared network activity upon the pharmacological block of GABA_A receptors by bicuculline application. In neural networks, the removal of the GABAergic synaptic component is known to alter the emerging activity patterns,^[2,36,37] leading to a more intense and regular bursting.^[2,35,38] Figure 3A (right dotted traces), shows samples of fluorescence tracings of active cells in the presence of bicuculline (or 10×10^{-6} M gabazine, not shown, see methods). As expected, regular Ca²⁺ events were detected in both culturing groups, characterized by IEI of 8.0 ± 0.05 s in 3D PDMS cultures ($n = 218$ cells), a value significantly ($***p < 0.001$; Kolmogorov–Smirnov test) lower when compared to that of 3D PDMS-GR 14.2 ± 0.2 s, $n = 175$ cells; all data summarized in the cumulative distribution in Figure 3B, right plot). Disinhibited activity was defined, in both groups, by comparable, although higher than in control, CCF values (3D PDMS CCF 0.75 ± 0.03 ; 3D PDMS-GR 0.81 ± 0.03 , data not shown). This strengthens the hypothesis that the higher calcium episodes occurrences in 3D PDMS-GR in standard saline solutions might indicate a diverse contribution of the GABAergic drive to the network activity in the two groups.

To ascertain whether the observed changes in network dynamics emerged from the sole presence of graphene, independently from the 3D growth conditions, hippocampal cultures were grown on flat coverslips covered by a thin layer of graphene flakes (2D GR, see the Experimental Section) and the emerging activity was compared to cells grown on flat glass coverslips (CTRL). In the standard saline solution, we detected 44% spontaneously active cells in 2D control conditions, increased to 52% in 2D GR. Figure 4A (left) shows representative visual fields of fluorescent cells and representative fluorescent tracings (right) of spontaneous and bicuculline-induced neuronal activity (dotted traces) recorded from 2D CTRL (top) and 2D GR (bottom) cultures. When we measured Ca²⁺ activity, the IEI was significantly ($***p < 0.001$; Kolmogorov–Smirnov test) lower in 2D GR cultures (9.2 ± 0.16 s, $n = 185$ cells, from 3 different series of cultures) when compared to control ones (14.7 ± 0.28 s, $n = 232$ cells, from 3 different series of cultures; see cumulative distributions in Figure 4B, left plot), in line with the reported increase in neuronal activity when cultures grow interfaced to single-layer graphene.^[8] The trend in terms of IEI in 2D graphene was preserved also in the presence of

bicuculline (13.4 ± 0.09 s, $n = 258$ cells, control; 7.4 ± 0.07 s, $n = 197$ cells, 2D GR; $***p < 0.001$; see cumulative distribution in Figure 4B, right plot). These results suggest that neurons, when interfaced to graphene, increased their activity but, differently from the 3D condition, the inhibitory control of the network was unaltered by graphene interfacing.

To acquire a better understanding of our observations, we investigated whether the 3D PDMS-GR scaffolds affected the development of inhibition in the resulting 3D neuronal circuits by considering two hypotheses. First, graphene might have changed the ratio of excitatory to inhibitory neurons altering the expression of the GABAergic neuronal phenotype. To validate this possibility 3D cultures developed inside 3D PDMS and 3D PDMS-GR scaffolds were coimmunostained with β -tubulin III and anti-GABA and processed by confocal microscopy (Figure 5A, left and right images, respectively). By quantifying the percentage of double positive cells, i.e., GABAergic neurons, for the two conditions we discovered that the two values were similar for 3D PDMS (40.3%, $n = 27$ visual fields, from 4 different series of cultures) and 3D PDMS-GR (43.2%, $n = 25$ visual fields, from 4 different series of cultures; summarized in the bar plot of Figure 5B).

The second hypothesis we investigated was that 3D PDMS-GR could have affected the maturation of GABAergic inhibition via tuning chloride ion fluxes through GABA_A receptors. It is, in fact, well known that during CNS development, neuronal intracellular chloride concentration shifts from higher to lower values (in respect to the extracellular one), modulating the amplitude of GABAergic currents.^[39,40] In accordance, in immature neurons, GABA_A receptors activation may result in a depolarization contributing to network bursting.^[41] We performed chloride imaging using a quinoline-based Cl⁻ indicator dye: MQAE (N-[6-methoxyquinolyl] acetoethyl ester).^[8,42] Figure 6A shows representative visual fields of MQAE-labeled neurons, in 3D PDMS (left) and 3D PDMS-GR (right) cultures. As shown in Figure 6B (tracings from 2 representative cells), when GABA (10×10^{-3} M; 10–20 s) is applied to 9–11 DIV cultures, efflux or influx of Cl⁻ are induced in the neurons, depending on their maturation, resulting in opposite changes in the Cl⁻ sensitive MQAE fluorescence.^[8] In all imaged fields ($n = 13$ for both condition), cells displaying opposite directions of GABA-evoked Cl⁻ fluxes were detected, thus confirming that immature and mature GABAergic phenotypes coexist within the same network. Anyhow, as shown in the plot of Figure 6B, the majority of the 3D PDMS neurons responded to GABA applications with a Cl⁻ influx, resulting in a decreased fluorescence signal due to dye quenching (plain trace at the bottom). The opposite condition was observed, instead, in the majority of neurons developed interfaced to the graphene within 3D PDMS-GR scaffolds (dotted line at the top, striped part of the histograms on the right).

3. Discussion

In basic neuroscience, 2D cultures represent a powerful platform that has allowed unraveling the mechanistic features of neurons and synapses. Yet they are limited tools when investigating the role of circuit topology on network dynamics,

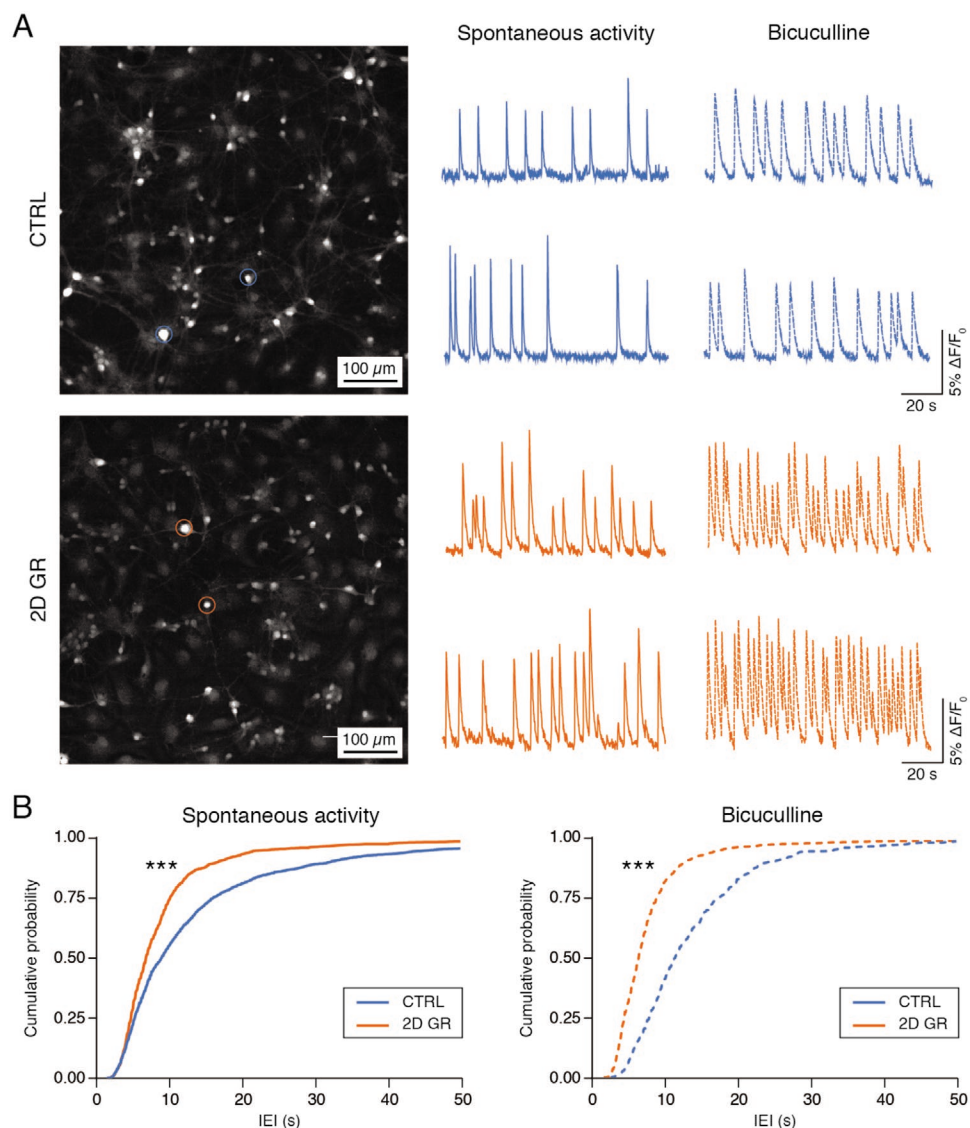


Figure 4. Live calcium imaging of hippocampal network in 2D controls and 2D-GR. A) Snapshots of representative fields of hippocampal cultures grown on 2D controls (CTRL) and 2D graphene (2D GR) stained with Oregon Green 488-BAPTA-1 AM Ca²⁺-dye. Fluorescence tracings represent repetitive Ca²⁺-events spontaneously (plain traces) or bicuculline induced (dotted traces) recorded in hippocampal cultures (two sample neurons were selected from the same field) in the two culturing conditions (CTRL, in blue; 2D GR, in orange). B) Cumulative probability plots of the interevent interval (IEI) values distribution in CTRL and 2D GR neurons in saline solution (left) and upon removal of synaptic inhibition by bicuculline (right). (Kolmogorov–Smirnov test; 3 different series of cultures; ****p* < 0.001.)

for example, when neuronal branches are exposed to the 3D space.^[2,3] Besides, 3D platforms, when compared to 2D ones, were shown to impact neuronal differentiation,^[9,43,44] cell and axonal growth,^[45,46] circuit functional organization and synaptic network synchronization.^[2] Further engineering of 3D scaffolds into CNS regenerative interfaces may be pursued by the use of nanomaterials, such as carbon-based ones, to improve the device's electrical conductivity and to favor the development of excitable tissue.^[7,22,47–49] Here, we exploit elastomeric 3D platforms to investigate the impact on network dynamics of posing at the interface few-layer graphene, known to affect cell signaling when supporting 2D cultures.^[8] The macroscopic stiffness of the 3D scaffolds we have fabricated was about 60 kPa, not so far from compliance values of rodent and human

brains (Young's moduli falling in the range of 0.1–20 kPa).^[50] The extremely high values of resistivity of the 3D PDMS-GR scaffold (in the MΩ mm range, at best) despite the presence of few-layers graphene flakes (whose electrical resistivity is in the order of 10–6 Ω mm)^[51,52] may result from the combined effects of the large contact resistances taking place between contiguous graphene flakes and the fact that graphene is not distributed in bulk inside the PDMS but it is randomly distributed on the scaffold's facets. The latter point implicates that the flat gold electrodes we have used to electrically characterize the material have a minimal contact area with graphene being, in the majority, in contact with PDMS, which is an insulator. Importantly, cells inside the scaffold developed in contact with the graphene flakes consequently, they locally experienced the

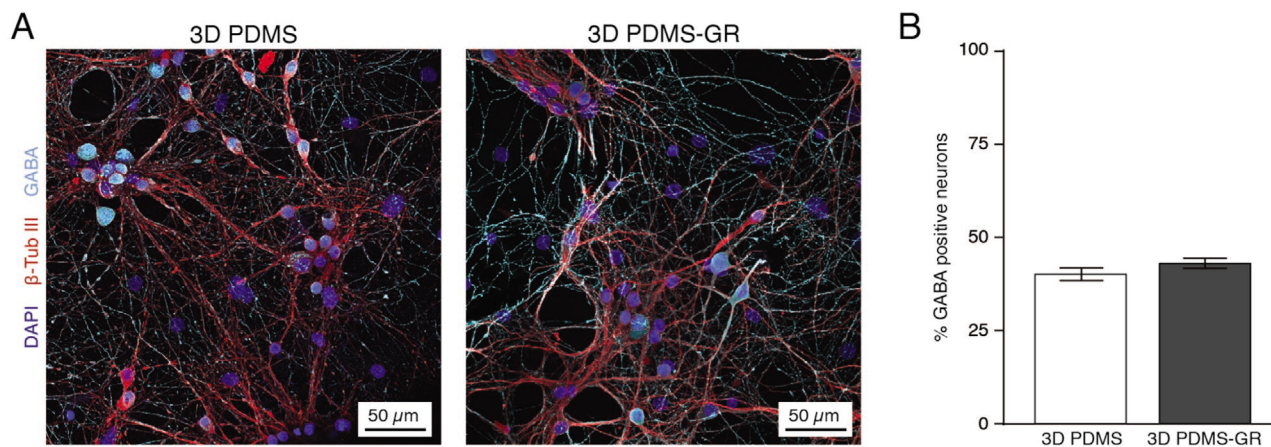


Figure 5. Expression of GABA phenotype in 3D PDMS and 3D PDMS-GR cultures. A) Confocal reconstructions of 3D PDMS (left) and 3D PDMS-GR (right) cultures coimmunostained against the neuronal marker β -tubulin III (in red) and a phenotypic-specific marker anti-GABA (in cyan). Cell nuclei were pointed out by DAPI (in dark blue). B) Bar plot summarizing the percentage of GABA-positive cells within the total neuronal population.

intrinsic low resistivity of this nanomaterial. This supposition is supported by the perturbation of neuronal network electrical activity we observed that is very similar to the effect induced on neuronal cells by single layer graphene.^[8]

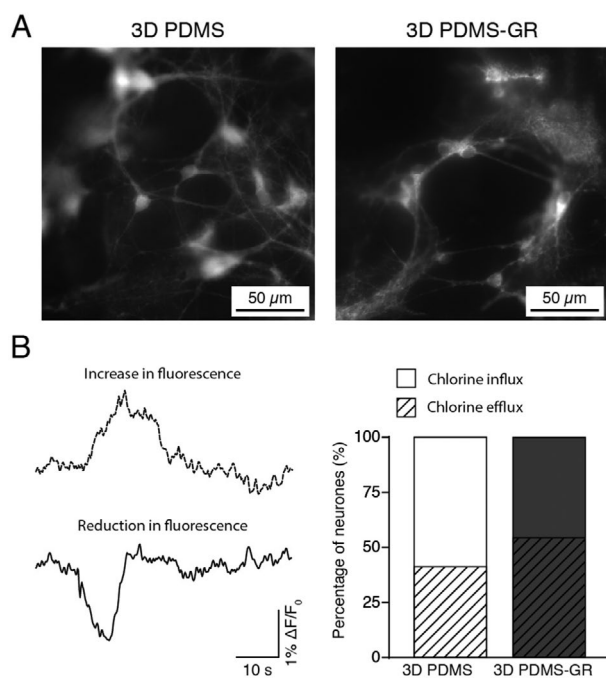


Figure 6. Live chloride imaging of hippocampal network in 3D PDMS and 3D PDMS-GR cultures. A) Representative visual fields of MQAE-labeled neurons of belonging to neuronal networks developed within a 3D PDMS scaffold (left) and a 3D PDMS-GR scaffold (right). B) At the left, fluorescent tracings representing chloride efflux (dotted trace corresponding to an increase in the detected fluorescence signal) or influx (plain trace corresponding to a reduction of the detected fluorescence signal) observed in two different cells, depending on their degree of maturation. At the right, a bar plot summarizing the percentage of neurons in 3D PDMS and in 3D PDMS-GR that, following GABA application, displayed a chloride influx (mature GABAergic neurons, plain areas) or, on the contrary, a chloride efflux (immature GABAergic neurons, striped areas).

We successfully reconstructed neuronal networks inside 3D PDMS and 3D PDMS-GR. In both growth conditions, neurons and GFAP-positive cells percolated the thickness of the scaffolds, generating healthy 3D networks of comparable size in the two constructs,^[2] being hippocampal cell densities and the neuron to glia ratio not affected by graphene layering. By live calcium imaging, we simultaneously monitor the activity of small groups of neurons. We detect episodes of intracellular calcium rise to measure the occurrence of neuronal and synaptic activity, a notion supported by TTX experiments.^[2] In 3D constructs, neuronal calcium episodes are usually due to brief synchronous firing, leading to transient synchronization of synaptic events.^[2,5] These bursts are accepted index of network dynamics,^[2,35] even in the absence, in calcium imaging, of single action potentials or individual synaptic currents resolution. The 3D architecture of synaptic connections sustained a high rate of bursting in 3D PDMS, confirming previous results where we postulated that 3D network topology favors neuronal connectivity efficiency.^[2] Spontaneous bursting was further increased in 3D PDMS-GR, potentially due to higher neuronal excitability or augmented neuronal connectivity, given the substantial similarities in network size with or without graphene. Indeed, 2D monoatomic layer of graphene was shown to improve cellular excitability via tuning the distribution of extracellular ions at the interface with neurons, leading to cell biophysical changes.^[8] In accordance, in our experiments with 2D graphene, the upscaled circuit excitability was observed in active cells involved in spontaneous and disinhibited bursting. On the contrary, the similar probability of finding spontaneously active neurons among 3D PDMS and 3D PDMS-GR fields does not support a mere increase in cell excitability or neuronal connectivity,^[2,53] and the slower pace of disinhibited rhythms in the presence of graphene is more suggestive of adaptive changes in the excitation/inhibition ratio, potentially following graphene interfacing in 3D configurations. We thus favor an alternative hypothesis, where the combination between synapse formation under 3D architecture and graphene interfaces affected the maturation of GABAergic inhibition, tuning the balance between hyperpolarizing and depolarizing responses, the latter

acting in synergy with glutamate and potentially contributing to network synchronization,^[41] in the absence of changes in GABAergic phenotype expression. We cannot exclude, however, that graphene, when engineered in a 3D configuration, might tune neuronal excitability by changing the ion adsorption at the neuronal/graphene interfaces, modifying membrane-associated neuronal functions.^[8]

Physical interactions between cells and the artificial materials on which they grow may influence biological behaviors and trigger growth, maturation, or differentiation.^[22,47–49,54] In the case of 3D PDMS-GR the mechanisms responsible for the (slight) network redistribution of inhibition maturation are not known and might include a complex interplay of mechanical, chemical, and electrical cues imposed by graphene when cells develop in the third dimension. Regardless of the need for future mechanistic studies resolving the effects of few-layer graphene in 3D constructs, our report suggests the importance of controlling the physicochemical properties of 3D scaffolds for the successful specialized guidance of neural network formation and function.

4. Conclusion

In this work, we exploited material science strategies to manufacture 3D scaffolds enabling the formation of neuronal circuits in the third dimension. We further introduced, by a simple and reproducible procedure, graphene flakes to interface neurons within the 3D structures. Innovative methods to introduce graphene in interfacing devices may improve the long-term stability of ultrasensitive electronic devices. On the other hand, graphene and graphene-based materials are attractive nanoplatforms for regenerative medicine approaches in neural tissue injury. Within this framework, we describe the ability of graphene to modulate neuronal circuit formation when interfaced in the third dimension. The possibility to govern cell neurobiology by nanomaterials' physical and topographical properties can be of interest in future 3D regenerative interfaces for long term medical developments.

5. Experimental Section

Graphene Preparation and Characterization: Graphene used for the scaffold preparation was obtained by a ball-milling protocol, as previously described.^[25] Briefly, 7.5 mg of graphite (Bay Carbon, Inc., USA) and 22.5 mg of melamine (Sigma-Aldrich) were ball-milled at 100 rpm for 30 min using a Retsch PM 100 planetary mill (Retsch Technology GmbH, Germany) under air atmosphere. The resulting solid was dispersed in water (20 mL), obtaining a dark suspension. Melamine was afterward removed by washing with hot water, and a precipitate consisting of poorly exfoliated graphite was removed from the liquid fraction after stabilization for 5 days.

The obtained graphene was subsequently fully characterized by TGA, Raman spectroscopy, and TEM techniques. TGA was performed at 10 °C min⁻¹ under nitrogen flow using a TGA Q50 (TA Instruments). About 20 graphene samples were analyzed by Raman spectroscopy using a Renishaw inVia Raman microspectrophotometer. The laser wavelength and the objective used were 532 nm and 100×, respectively. The morphology and the lateral size of so obtained graphene flakes were obtained by a Jeol JEM 1011 transmission electron microscope and analyzed using ImageJ open-source software to calculate sheets dimensions.^[55]

Sample Fabrication and Characterization: Flat glass control (CTRL) substrates were commercial glass coverslips (12 × 24 mm²) cleaned in “piranha solution” (H₂SO₄:H₂O 3:1, 100 mL for 50 coverslips) at 90 °C for 16 h. Before use, samples were carefully rinsed with deionized water and left to dry in an oven at 80 °C overnight.

Flat graphene samples (2D GR) were prepared depositing by spray-coating a thin homogeneous film of few-layer graphene flakes on glass control substrates (see Figure S1 in the Supporting Information). Briefly, substrates were placed on a hot plate at 100 °C and were sprayed with an ethanol dispersion of graphene flakes (0.05 mg mL⁻¹) using a Junior 140 airbrush (SAGOLA, Spain) until reaching a sheet resistance of about 150 kOhm Ω⁻¹. The distance between the airbrush and the plate was around 20 cm, and the nitrogen pressure used to spray was 2 bars. The substrates were then placed in an oven at 350 °C for 20 min to remove any trace of solvent. Finally, sheet resistance and transmittance (550 nm) were measured using a 34461A Agilent Bench Multimeter (Agilent Technologies, Inc., USA) and a Cary 5000 UV–vis–NIR spectrophotometer (Agilent Technologies, Inc., USA). The final graphene films were characterized by an average sheet resistance of 30.4 kOhm Ω⁻¹ and an average transmittance of 37%. Scanning electron microscopy was performed using a Philips XL30 system after samples were coated with a 3 nm layer of gold (Figure S1, Supporting Information).

Self-standing elastomeric scaffolds (3D PDMS-GR) with all facets decorated with flakes of graphene were obtained by shaking overnight and in dry conditions a mixture of graphene (30 mg) and sucrose (500 mg, sieved to have a granulometry of 125–250 μm). Subsequently, 20 μL of deionized water was added and mixed, obtaining a homogeneously wet mixture. The mixture was molded into the desired shape (a 5 × 5 × 15 mm³ edges parallelepiped), gently pressed and dried at 60 °C. Polydimethylsiloxane (PDMS—SYLGARD 184 Silicone Elastomer from Dow Corning) was prepared and layered with a thickness of 5 mm in a glass dish. The sugar/graphene solid conglomerate was placed onto the dish and was infiltrated under vacuum with PDMS. The cubes were then cured in an oven at 85 °C for 1 h and cooled at room temperature. PDMS excess was trimmed away and the cube was dipped in distilled water to dissolve the sugar. 3D PDMS control samples were prepared following the same protocol but in the absence of graphene.

Elastomeric scaffold containing few-layer graphene was further characterized by Raman spectroscopy. Raman spectra of 3D PDMS-GR were recorded with an InVia Renishaw microspectrometer equipped with a 532 nm point-based laser. The power density was kept in all cases below 5 mW μm⁻² to avoid laser-over heating effects. The obtained spectra were a result of probing 25 random locations on the sample. 3D Raman mappings were performed with the 532 nm laser by using the line-based option (streamline), which analyzed rectangular slices of sample and depth steps of 1 μm until reaching 10 μm allowing to map the G-band intensities in three dimensions. 3D PDMS and 3D PDMS-GR scaffold morphologies were evaluated through SEM. Images were collected on a Gemini SUPRA 40 SEM (Carl Zeiss GmbH, Germany) collecting secondary electrons mounting 250 μm thick slices of the bare scaffolds with conductive carbon tape (Ted Pella, Inc., USA). Images were acquired at 2.5 keV accelerating voltage. Before SEM characterization, both samples were Au metalized with a metal sputter coater (Polaron SC7620). For the mechanical characterization of the 3D PDMS-GR microporous scaffold, a compressive test was performed. In this, cubic samples with a dimension of 5 mm in side was used. Tests were performed taking advantage of a Galdabini SUN 500 uniaxial microcompression apparatus. Scaffolds were compressed between two circular (20 mm in diameter) flat surfaces using a high sensitivity load cell for data acquisition (CTCA10K5, AEP Transducers, Italy). All tests were done in air at room temperature. Before starting the test, a 50 mN preload was applied to the sample to ensure good contact between the sample and the two pressing surfaces. 10 μm s⁻¹ constant speed loading cycle was used with a final load limit fixed at 1 N. Final compressive displacement was about 2 mm (40%). Each representative stress–strain curve was obtained by averaging the results from at least 5 measurements. Sample stiffness was determined as

Young's Modulus (E) evaluating the slope of the linear portion of the stress-strain curve (roughly from 10% to 25% deformation). Graphene-based scaffold electrical characteristic was studied placing a 5 mm side size cube of the 3D PDMS-GR scaffold between two conductive coplanar flat gold electrodes ($10 \times 10 \text{ mm}^2$) on a home-made device. The sample was initially squeezed between the two electrodes at a constant 50 mN load to assure optimal contact. Resistivity was assessed using a low current source-meter (KEITHLEY 2601A System SourceMeter) at an applied bias voltage of about 20 V. The dependence of the resistance upon deformation was determined at steps of 10% up to 60% total deformation. All electrical measurements were carried out at room temperature in air. The deformation-dependent resistivity plot was obtained by averaging the results from three different samples and was calculated from the resistance via scaffold's geometrical characteristics.

Cell Culture Preparation: Isolation of primary hippocampal tissue was operated in agreement with the guidance of the National Institutes of Health and with the proper international and institutional standards for the care and use of animals in research (Italian Ministry of Health, in agreement with the EU Recommendation 2007/526/CE). All procedures were approved by the local veterinary authorities and performed following the Italian law (decree 26/14) and the UE guidelines (2007/526/CE and 2010/63/UE). The animal use was approved by the Italian Ministry of Health. All efforts were made to reduce the number of animals used and to minimize animal suffering. All the reagents were purchased from Sigma-Aldrich if not otherwise indicated. Dissociated hippocampal cultures were prepared from postnatal 2–3 days old (P2–P3) Wistar rats, as previously reported.^[2,30] Cells were plated on four distinct substrates: poly-L-ornithine coated glass coverslips (CTRL), graphene flakes coated glass coverslips (2D GR), pristine 3D scaffolds (3D PDMS), and 3D, graphene functionalized, scaffolds (3D PDMS-GR). 3D scaffolds were sliced with a thickness of about 400 μm and then mounted on the glass coverslips using a slight adhesive PDMS layer cured for 1 h at 120 °C.^[2,9] One-hour prior to cell plating, in order to promote cell adhesion, 2D GR, 3D PDMS, and 3D PDMS-GR samples were exposed to low-pressure air plasma (Harrick PDC-32G Plasma Cleaner) for 5 min at room temperature (20–22 °C) and finally sterilized with ultraviolet (UV) radiations for 20 min.^[2] Cultures were incubated at 37 °C, 5% CO₂ in a culture medium consisting of MEM (Gibco) containing 35 $\times 10^{-3}$ M glucose (Carlo Erba Reagents), 15 $\times 10^{-3}$ M 4-(2-hydroxyethyl)-1-piperazineethanesulfonic acid (HEPES), 1 $\times 10^{-3}$ M Apo-Transferrin, 48 $\times 10^{-3}$ M Insulin, 3 $\times 10^{-3}$ M Biotin, 1 $\times 10^{-3}$ M Vitamin B12, 500 $\times 10^{-9}$ M Gentamicin (Gibco) was also added to prevent contamination. Half of the culture medium was renewed two days after seeding and then changed every two days. Cultures were grown for 9–11 days in vitro (DIV) and then used for experiments.^[2]

Immunofluorescence: Cells cultured in 3D PDMS and 3D PDMS-GR Scaffolds were fixed in 4% formaldehyde (prepared from fresh paraformaldehyde) in PBS 1 \times for 30 min and 1% glutaraldehyde for 1 h for GABA staining, as previously reported.^[56] Cultures were permeabilized for 45 min with 0.3% Triton-X-100 (Carlo Erba) in PBS and subsequently incubated with primary antibodies for 45 min at RT. After being washed, samples were finally incubated with secondary antibodies for 45 min. Samples were mounted with antifade medium Fluoromount on 1 mm thick microscope glass slides. Neurons were stained with rabbit anti- β -tubulin III primary antibody (1:500 dilution) and visualized with Alexa 594 goat antirabbit as the secondary antibody (1:500, Invitrogen). Astrocytes were labeled with mouse anti-GFAP primary antibodies (1:250) and visualized with Alexa 488 antimouse in goat as the secondary antibody (1:500, Invitrogen).

For GABA immunostaining, mouse anti- β -tubulin III (1:500) and rabbit anti-GABA (1:300 dilution) were used as primary antibodies while Alexa 594 goat anti-mouse (1:500) and Alexa 488 goat anti-rabbit (1:500 dilution) as secondary antibodies. Nuclei were stained in all conditions with 4',6-diamidino-2-phenylindole (DAPI, 1:200, Invitrogen). Graphene was visualized by reflection mode during the confocal acquisition.^[57,58] To evaluate the density of neurons and astrocytes, immunolabeled 3D cultures were analyzed using an inverted confocal microscope (Nikon, Japan), acquiring serial confocal planes (z-stack) every 1 μm across the entire 3D sections. Moreover, to quantify the percentage of GABA-

positive neurons, images were acquired with 40 \times objective (0.75 NA, PlanFluor, Nikon, Japan; z-stack every 500 nm) from randomly selected fields, and double β -tubulin III- and GABA-positive neurons were counted (3D PDMS: $n = 27$ visual fields, from 4 different series of cultures; 3D PDMS-GR: $n = 25$ visual fields, from 4 different series of cultures). The total amount of double-positive neurons (i.e., GABAergic ones) was then normalized to the overall number of neurons (β -tubulin III positive cells) visualized in each visual field. Analysis and images reconstruction were accomplished using open-source ImageJ software.^[55]

Live Cell Imaging: For calcium (Ca²⁺) imaging experiments, hippocampal cultures were loaded with the cell-permeable Ca²⁺ indicator Oregon Green 488 BAPTA-1 AM (Molecular Probes). Dissociated cultures were incubated for 45 min at 37 °C, 5% CO₂ at a final indicator concentration of 4 $\times 10^{-6}$ M. Subsequently samples were placed in a recording chamber mounted on an inverted microscope (Nikon Eclipse Ti-U) and continuously perfused at RT and at 5 mL min⁻¹ with a recording solution of composition: 150 $\times 10^{-3}$ M NaCl, 4 $\times 10^{-3}$ M KCl, 2 $\times 10^{-3}$ M CaCl₂, 1 $\times 10^{-3}$ M MgCl₂, 10 $\times 10^{-3}$ M HEPES, 10 $\times 10^{-3}$ M glucose (pH adjusted to 7.4 with NaOH; osmolarity 300 mOsm). The Oregon Green loaded cultures were observed with a 20 \times objective (PlanFluor, 0.45 NA, Nikon, Japan) using an ORCA-Flash 4.0 V2 sCMOS camera (Hamamatsu). Images were acquired at a sampling rate of 6.67 Hz (150 ms exposure time) under continuous illumination. The camera was set to operate at 512 \times 512 pixels. The Ca²⁺ dye was excited at 488 nm using appropriate filters/dichroic cube set and a mercury (Hg) lamp (Nikon Intensilight). The excitation light was attenuated by neutral density filters (ND 32). Images from collected light were acquired by an integrating imaging software package (HCLImage Live, Hamamatsu). After recording the spontaneous activity of hippocampal neurons for 10–15 min, 10 $\times 10^{-6}$ M bicuculline or 10 $\times 10^{-6}$ M gabazine (both GABA_A antagonist) were applied to the bath for 20 min. At the end of each experiment, 1 $\times 10^{-6}$ M TTX (a voltage-gated, fast Na⁺ channel blocker; Latoxan) was added to the recording solution to confirm the neuronal nature of the recorded signals. For each sample, from each field, individual (not overlapping or interfering) 30 \pm 12 cells were recorded by drawing regions of interest (ROIs) around clearly recognizable cell bodies. The corresponding light intensity traces were analyzed with Clampfit software (pClamp suite, 10.4 version; Axon Instruments) in off-line mode and with Igor Pro Software (6.32 A version; WaveMetrics, Lake Oswego, OR, USA). The difference between consecutive onset times was then computed to obtain the IEI. Once the IEI values were measured from each active cell in the field, data were pooled for all fields recorded under the same experimental conditions and averaged for further comparison. Intracellular Ca²⁺ transients were expressed as fractional amplitude increase ($\Delta F/F_0$, where F_0 is the baseline fluorescence level and ΔF is the rise over baseline). The onset time of neuronal activation was determined by detecting those events in the fluorescence signal that exceed at least five times the standard deviation of the noise.^[2] The values of CCF were evaluated using a home-made procedure in Igor Pro and used to measure the strength of the correlation between cells (i.e., the relative probability that the peaks of calcium transients took place at the same time in all the cells of a certain field). For chloride imaging, hippocampal dissociated cultures grown within 3D scaffolds were loaded with the fluorescent chloride indicator *N*-[6-methoxyquinolyl] acetoethyl ester (MQAE), 1 $\times 10^{-3}$ M final concentration, from Abcam) diluted in the recording solution for 10 min at 37 °C.^[42] After 10 min washes, each sample was placed in a recording chamber mounted on an inverted microscope (Nikon Eclipse Ti-U) and observed with a 60 \times objective (0.7 NA, PlanFluor, Nikon, Japan). Samples were continuously perfused at RT and at 5 mL min⁻¹ with a recording solution (see above the composition). Images were acquired using an ORCA-Flash 4.0 V2 sCMOS camera (Hamamatsu) for 1 min at 5 Hz (200 ms exposure time). The fluorescent chloride indicator was excited at the 365 nm Hg peak using a UV-2A Nikon filter set while excitation light was attenuated by a neutral density filter (ND 16). The imaging system was controlled by the integrating imaging software (HCLImage Live, Hamamatsu) and the camera was set to operate on 1024 \times 1024 pixels. After 5 s from the beginning of the recording, 10 $\times 10^{-3}$ M GABA was bath-applied for 20 s to evoke chloride influx/efflux through the membrane.

Image time stacks were analyzed in selected ROI to evaluate the variations in MQAE fluorescence intensity. Images were analyzed by ImageJ software (NIH) and the corresponding traces were studied with Clampfit software (pClamp suite, 10.4 version; Axon Instruments) in off-line mode and with Igor Pro Software (6.32 A version; WaveMetrics, Lake Oswego, OR, USA). The number of neurons responding with an increase or a decrease in fluorescence was quantified and normalized to the total number of neurons responding to GABA application in each visual field. Intracellular Cl⁻ transients were expressed as fractional amplitude variations ($\Delta F/F_0$) and selected only when exceeded at least five times the standard deviation of the noise.^[8]

Statistical Analysis: All values from samples subjected to the same experimental protocols were pooled together and expressed as mean \pm s.e.m., with n = number of cells, if not otherwise indicated. Sample size was reported within the results and/or methods regarding each experimental set, all data were collected from ≥ 3 culture series. D'Agostino and Pearson omnibus normality test was applied to evaluate the statistical distribution of the data sets. The statistically significant difference between two data sets was assessed by Student's t -test for parametric data and by Mann–Whitney or Kolmogorov–Smirnov test for nonparametric ones. Statistical significance was determined at $p < 0.05$, unless otherwise indicated. Significance was graphically indicated as follows: * $p < 0.05$, ** $p < 0.01$, and *** $p < 0.001$.

Supporting Information

Supporting Information is available from the Wiley Online Library or from the author.

Acknowledgements

The authors are especially grateful to Micaela Gandolfo for supervising the confocal image reconstruction, to Livia Piatti and Gianluca Turco for characterizing the material compressibility. IOM-TASC National Laboratory (Trieste) is also gratefully acknowledged for SEM assistance. The authors also wish to thank the IRICA Institute for the use of their shared equipment, services, and expertise. The authors acknowledge financial support from the European Union's Horizon 2020 research and innovation program under Grant Agreements 785219 Graphene Flagship. This work was also supported by the Spanish Ministry of Economy and Competitiveness MINECO (projects CTQ2017-88158-R and CTQ2016-76721-R), by the University of Trieste, and Consorzio Interuniversitario Nazionale per la Scienza e Tecnologia dei Materiali (INSTM). M.P., as the recipient of the AXA Chair, is grateful to the AXA Research Fund for financial support. This work was performed under the Maria de Maeztu Units of Excellence Program from the Spanish State Research Agency – Grant No. MDM-2017-0720

Conflict of Interest

The authors declare no conflict of interest.

Author Contributions

The manuscript was written through contributions of all authors. All authors have given approval to the final version of the manuscript.

Keywords

3D-scaffolds, graphene, hippocampal network, neuronal maturation

Received: September 24, 2019

Revised: January 19, 2020

Published online: February 19, 2020

- [1] A. Gladkov, Y. Pigareva, D. Kutiyina, V. Kolpakov, A. Bukatin, I. Mukhina, V. Kazantsev, A. Pimashkin, *Sci. Rep.* **2017**, *7*, 15625.
- [2] S. Bosi, R. Rauti, J. Laishram, A. Turco, D. Lonardoni, T. Nieuws, M. Prato, D. Scaini, L. Ballerini, *Sci. Rep.* **2015**, *5*, 9562.
- [3] F. P. Ulloa Severino, J. Ban, Q. Song, M. Tang, G. Bianconi, G. Cheng, V. Torre, *Sci. Rep.* **2016**, 29640.
- [4] E. R. Aurand, S. Usmani, M. Medelin, D. Scaini, S. Bosi, F. B. Rosselli, S. Donato, G. Tromba, M. Prato, L. Ballerini, *Adv. Funct. Mater.* **2018**, *28*, 1700550.
- [5] G. Cellot, E. Cilia, S. Cipollone, V. Rancic, A. Sucapane, S. Giordani, L. Gambazzi, H. Markram, M. Grandolfo, D. Scaini, F. Gelain, L. Casalis, M. Prato, M. Giugliano, L. Ballerini, *Nat. Nanotechnol.* **2009**, *4*, 126.
- [6] G. Cellot, F. M. Toma, Z. K. Varley, J. Laishram, A. Villari, M. Quintana, S. Cipollone, M. Prato, L. Ballerini, *J. Neurosci.* **2011**, *31*, 12945.
- [7] I. Rago, R. Rauti, M. Bevilacqua, I. Calaresu, A. Pozzato, M. Cibinel, M. Dalmiglio, C. Tavagnacco, A. Goldoni, D. Scaini, *Adv. Biosyst.* **2019**, *3*, 1800286.
- [8] N. P. Pampaloni, M. Lottner, M. Giugliano, A. Matruglio, F. D'Amico, M. Prato, J. A. Garrido, L. Ballerini, D. Scaini, *Nat. Nanotechnol.* **2018**, *13*, 755.
- [9] C. Martín, S. Merino, J. M. González-Domínguez, R. Rauti, L. Ballerini, M. Prato, E. Vázquez, *Sci. Rep.* **2017**, *7*, 10942.
- [10] V. C. Sanchez, A. R. Jachak, H. Hurt, A. B. Kane, *Chem. Res. Toxicol.* **2012**, *25*, 15.
- [11] K. Kostarelos, K. S. Novoselov, *Science* **2014**, *344*, 261.
- [12] H. Y. Mao, S. Laurent, W. Chen, O. Akhavan, M. Imani, A. A. Ashkarran, M. Mahmoudi, *Chem. Rev.* **2013**, *113*, 3407.
- [13] M. C. Serrano, J. Patiño, C. García-Rama, M. L. Ferrer, J. L. G. Fierro, A. Tamayo, J. E. Collazos-Castro, F. del Monte, M. C. Gutiérrez, *J. Mater. Chem. B* **2014**, *2*, 5698.
- [14] L. Yichen, L. Xin, H. Ryoma, R. Chi, Z. Xingwang, K. Takaki, K. Duygu, *Adv. Funct. Mater.* **2018**, *28*, 1800002.
- [15] N. Li, X. Zhang, Q. Song, R. Su, Q. Zhang, T. Kong, L. Liu, G. Jin, M. Tang, G. Cheng, *Biomaterials* **2011**, *32*, 9374.
- [16] Q. Song, Z. Jiang, N. Li, P. Liu, L. Liu, M. Tang, C. Cheng, *Biomaterials* **2014**, *35*, 6930.
- [17] R. Rauti, M. Medelin, L. Newman, S. Vranic, G. Reina, A. Bianco, M. Prato, K. Kostarelos, L. Ballerini, *Nano Lett.* **2019**, *19*, 2858.
- [18] M. Tang, Q. Song, N. Li, Z. Jiang, R. Huang, G. Cheng, *Biomaterials* **2013**, *34*, 6402.
- [19] D. Bitounis, H. Ali-Boucetta, B. H. Hong, D. H. Min, K. Kostarelos, *Adv. Mater.* **2013**, *25*, 2258.
- [20] D. Kuzum, H. Takano, E. Shim, J. C. Reed, H. Juul, A. G. Richardson, J. de Vries, H. Bink, M. A. Dichter, T. H. Lucas, D. A. Coulter, E. Cubukcu, B. Litt, *Nat. Commun.* **2014**, *5*, 5259.
- [21] E. Masvidal-Codina, X. Illa, M. Dasilva, A. B. Calia, T. Dragojević, E. E. Vidal-Rosas, E. Prats-Alfonso, J. Martínez-Aguilar, J. M. De la Cruz, R. Garcia-Cortadella, P. Godignon, G. Rius, A. Camassa, E. Del Corro, J. Bousquet, C. Hébert, T. Durduran, R. Villa, M. V. Sanchez-Vives, J. A. Garrido, A. Guimerà-Brunet, *Nat. Mater.* **2019**, *18*, 280.
- [22] R. Rauti, M. Musto, S. Bosi, M. Prato, L. Ballerini, *Carbon* **2019**, *143*, 430.
- [23] N. Li, Q. Zhang, S. Gao, Q. Song, R. Huang, L. Wang, L. Liu, J. Dai, M. Tang, G. Cheng, *Sci. Rep.* **2013**, *3*, 1604.

- [24] A. Domínguez-Bajo, A. González-Mayorga, C. R. Guerrero, F. J. Palomares, R. García, E. López-Dolado, M. C. Serrano, *Biomaterials* **2019**, *192*, 461.
- [25] V. León, J. M. González-Domínguez, J. L. Fierro, M. Prato, E. Vázquez, *Nanoscale* **2016**, *8*, 14548.
- [26] C. Casiraghi, A. Hartschuh, H. Qian, S. Pisanec, C. Georgi, A. Fasoli, K. S. Novoselov, D. M. Basko, A. C. Ferrari, *Nano Lett.* **2009**, *9*, 1433.
- [27] K. R. Paton, E. Varrla, C. Backes, R. J. Smith, U. Khan, A. O'Neill, C. Boland, M. Lotya, O. M. Istrate, P. King, T. Higgins, S. Barwich, P. May, P. Puczkarski, I. Ahmed, M. Moebius, H. Pettersson, E. Long, J. Coelho, S. E. O'Brien, E. K. McGuire, B. M. Sanchez, G. S. Duesberg, N. McEvoy, T. J. Pennycook, C. Downing, A. Crossley, V. Nicolosi, J. N. Coleman, *Nat. Mater.* **2014**, *13*, 624.
- [28] U. Mogera, R. Dhanya, R. Pujar, C. Narayana, G. U. Kulkarni, *J. Phys. Chem. Lett.* **2015**, *6*, 4437.
- [29] D. Cai, A. Neyer, R. Kuckuk, H. M. Heise, *J. Mol. Struct.* **2010**, *976*, 274.
- [30] R. Rauti, N. Lozano, V. León, D. Scaini, M. Musto, I. Rago, F. P. Ulloa Severino, A. Fabbro, L. Casalis, E. Vázquez, K. Kostarelos, M. Prato, L. Ballerini, *ACS Nano* **2016**, *10*, 4459.
- [31] A. Càceres, G. A. Banker, L. Binder, *J. Neurosci.* **1986**, *6*, 714.
- [32] N. J. Willmott, K. Wong, A. J. Strong, *FEBS Lett.* **2000**, *487*, 239.
- [33] A. Fabbro, A. Villari, J. Laishram, D. Scaini, F. M. Toma, A. Turco, M. Prato, L. Ballerini, *ACS Nano* **2012**, *6*, 2041.
- [34] E. Marconi, T. Nieuw, A. Maccione, P. Valente, A. Simi, M. Messa, S. Dante, P. Baldelli, L. Berdondini, F. Benfenati, *PLoS One* **2012**, *7*, e34648.
- [35] O. Stetter, D. Battaglia, J. Soriano, T. Geisel, *PLoS Comput. Biol.* **2012**, *8*, e1002653.
- [36] D. M. Sokal, R. Mason, T. L. Parker, *Neuropharmacology* **2000**, *39*, 2408.
- [37] E. Tibau, M. Valencia, J. Soriano, *Front. Neural Circuits* **2013**, *7*, 1.
- [38] A. Fabbro, B. Pastore, A. Nistri, L. Ballerini, *Cell Calcium* **2007**, *41*, 317.
- [39] D. Arosio, G. M. Ratto, *Front. Cell. Neurosci.* **2014**, *8*, 258.
- [40] E. Cherubini, *Int. J. Dev. Neurosci.* **1990**, *8*, 481.
- [41] G. Cellot, L. Maggi, M. A. Di Castro, M. Catalano, R. Migliore, M. Migliore, M. L. Scattoni, G. Calamandrei, E. Cherubini, *Sci. Rep.* **2016**, *6*, 31696.
- [42] N. Marandi, A. Konnerth, O. Garaschuk, *Pflügers Arch.* **2002**, *445*, 357.
- [43] Y. Lee, J. M. Lee, P. K. Bae, I. Y. Chung, B. H. Chung, B. G. Chung, *Electrophoresis* **2015**, *36*, 994.
- [44] P. Moshayedi, L. R. Nih, I. Llorente, A. R. Berg, J. K. Cinkornpumin, W. E. Lowry, T. Segura, S. T. Carmichael, *Biomaterials* **2016**, *105*, 145.
- [45] T. B. Puschmann, Y. de Pablo, C. Zanden, J. Liu, M. A. Pekny, *Tissue Eng., Part C* **2014**, *20*, 485.
- [46] S. Usmani, E. R. Aurand, M. Medelin, A. Fabbro, D. Scaini, J. Laishram, F. B. Rosselli, A. Ansuini, D. Zoccolan, M. Scarselli, M. De Crescenzi, S. Bosi, M. Prato, L. Ballerini, *Sci. Adv.* **2016**, *2*, 1600087.
- [47] T. Dvir, B. P. Timko, M. D. Brigham, S. R. Naik, S. S. Karajanagi, O. Levy, H. Jin, K. K. Parker, R. Langer, D. S. Kohane, *Nat Nanotechnol.* **2011**, *6*, 720.
- [48] S. Marchesan, L. Ballerini, M. Prato, *Science* **2017**, *356*, 1010.
- [49] S. Scaini, L. Ballerini, *Curr. Opin. Neurobiol.* **2018**, *50*, 50.
- [50] W. J. Tyler, *Nat. Rev. Neurosci.* **2012**, *13*, 867.
- [51] N. Rouhi, Y. Y. Wang, P. J. Burke, *Appl. Phys. Lett.* **2012**, *101*, 263101.
- [52] A. N. Sruti, K. J. Jagannadham, *Electron. Mater.* **2010**, *39*, 1268.
- [53] F. Aguado, M. A. Carmona, E. Pozas, A. Aguiló, F. J. Martínez-Guijarro, S. Alcantara, V. Borrell, R. Yuste, C. F. Ibañez, E. Soriano, *Development* **2003**, *130*, 1267.
- [54] K. Kenry, W. C. Lee, K. P. Loh, C. T. Lim, *Biomaterials* **2018**, *155*, 236.
- [55] C. A. Schneider, W. S. Rasband, K. W. Eliceiri, *Nat. Methods* **2012**, *9*, 671.
- [56] F. Furlan, G. Taccola, M. Grandolfo, L. Guasti, A. Arcangeli, A. Nistri, L. Ballerini, *J. Neurosci.* **2007**, *27*, 919.
- [57] M. Bramini, S. Sacchetti, A. Armirotti, A. Rocchi, E. Vázquez, V. León Castellanos, T. Bandiera, F. Cesca, F. Benfenati, *ACS Nano* **2016**, *10*, 7154.
- [58] M. Musto, R. Rauti, A. F. Rodrigues, E. Bonechi, C. Ballerini, K. Kostarelos, L. Ballerini, *Front. Syst. Neurosci.* **2019**, *13*, 1.